

# Geophysical Research Letters

## RESEARCH LETTER

10.1029/2019GL082471

### Key Points:

- Electron crescent-shaped distributions produce upper hybrid waves in magnetotail reconnection events
- Field-aligned electron beams generate parallel electrostatic waves through the beam-mode
- Multiple crescent and convecting core distributions act together to produce broad frequency spectra as observed by MMS

### Supporting Information:

- Supporting Information S1

### Correspondence to:

J. L. Burch,  
jburch@swri.edu

### Citation:

Burch, J. L., Dokgo, K., Hwang, K. J., Torbert, R. B., Graham, D. B., Webster, J. M., et al. (2019). High-frequency wave generation in magnetotail reconnection: Linear dispersion analysis. *Geophysical Research Letters*, *46*, 4089–4097. <https://doi.org/10.1029/2019GL082471>














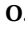

Received 14 FEB 2019

Accepted 30 MAR 2019

Accepted article online 3 APR 2019

Published online 23 APR 2019

## High-Frequency Wave Generation in Magnetotail Reconnection: Linear Dispersion Analysis

J.L. Burch<sup>1</sup> , K. Dokgo<sup>1</sup> , K.J. Hwang<sup>1</sup> , R.B. Torbert<sup>2,1</sup> , D.B. Graham<sup>3</sup> , J.M. Webster<sup>4</sup> , R.E. Ergun<sup>5</sup> , B.L. Giles<sup>6</sup> , R.C. Allen<sup>7</sup> , L.-J. Chen<sup>6</sup> , S. Wang<sup>8</sup> , K.J. Genestreti<sup>2</sup> , C.T. Russell<sup>9</sup> , R.J. Strangeway<sup>9</sup> , and O. Le Contel<sup>10</sup> 

<sup>1</sup>Southwest Research Institute, San Antonio, TX, USA, <sup>2</sup>Department of Physics, University of New Hampshire, Durham, NH, USA, <sup>3</sup>Swedish Institute of Space Physics, Uppsala, Sweden, <sup>4</sup>Department of Physics and Astronomy, Rice University, Houston, TX, USA, <sup>5</sup>LASP, University of Colorado Boulder, Boulder, CO, USA, <sup>6</sup>NASA, Goddard Space Flight Center, Greenbelt, MD, USA, <sup>7</sup>Applied Physics Laboratory, The Johns Hopkins University, Laurel, MD, USA, <sup>8</sup>Department of Astronomy, University of Maryland, College Park, MD, USA, <sup>9</sup>Earth and Planetary Sciences, University of California, Los Angeles, CA, USA, <sup>10</sup>Laboratoire de Physique des Plasmas, CNRS, Ecole Polytechnique, Sorbonne Université, Université Paris-Sud, Observatoire de Paris, Paris, France

**Abstract** Plasma and wave measurements from the NASA Magnetospheric Multiscale mission are presented for magnetotail reconnection events on 3 July and 11 July 2017. Linear dispersion analyses were performed using distribution functions comprising up to six drifting bi-Maxwellian distributions. In both events electron crescent-shaped distributions are shown to be responsible for upper hybrid waves near the X-line. In an adjacent location within the 3 July event a monodirectional field-aligned electron beam drove parallel-propagating beam-mode waves. In the 11 July event an electron distribution consisting of a drifting core and two crescents was shown to generate upper-hybrid and beam-mode waves at three different frequencies, explaining the observed broadband waves. Multiple harmonics of the upper hybrid waves were observed but cannot be explained by the linear dispersion analysis since they result from nonlinear beam interactions.

**Plain Language Summary** Magnetic reconnection is a process that occurs throughout the universe in ionized gases (plasmas) containing embedded magnetic fields. This process converts magnetic energy to electron and ion energy, causing phenomena such as solar flares and auroras. The NASA Magnetospheric Multiscale mission has shown that in magnetic reconnection regions there are intense electric field oscillations or waves and that electrons form crescent and beam-like populations propagating both along and perpendicular to the magnetic field. This study shows that the observed electron populations are responsible for high-frequency waves including their propagation directions and frequency ranges.

## 1. Introduction

Investigations of magnetic reconnection at the dayside magnetopause by the NASA Magnetospheric Multiscale (MMS) mission (Burch, Moore, et al., 2016) have shown that agyrotropic “crescent” electron distributions (Burch, Torbert, et al., 2016) and magnetic field-aligned electron beams (Burch & Phan, 2016) occur in the electron stagnation region and near the X-line, respectively. Detection of these distributions benefits from the high time resolution of the MMS electron measurements (3-D in 30 ms) provided by the Fast Plasma Investigation (Pollock et al., 2016). In addition to carrying the out-of-plane current required for reconnection, these electron distributions have also been shown to generate intense waves, for example, upper hybrid (UH) and Langmuir waves, near the electron plasma frequency (Burch, Ergun, et al., 2018; Graham et al., 2017) and Bernstein waves between harmonics of the electron cyclotron frequency (Graham et al., 2018). Graham et al. (2018) have derived the occurrence patterns of Langmuir waves and UH waves along the entire dayside magnetopause with the occurrence probability of UH waves being the highest.

Farrell et al. (2002) used WIND data from the tail reconnection event published by Øieroset et al. (2001) to show that intense UH waves occurred in the near vicinity of the X-line. Electron distribution functions (DFs) in this region were analyzed by Farrell et al. (2003), showing beams of electrons flowing along the reconnection separatrices toward the X-line as predicted from the simulations and Geotail

observations of Hoshino et al. (2001). A dispersion analysis by Farrell et al. (2003) showed that the electron beams have sufficient  $df/dv_{par}$  to drive UH waves. Other features of the Farrell et al. electron distributions were a secondary beam at lower energies flowing away from the X-line and a “football” distribution (Hoshino et al., 2001) that results from wave-particle interactions and acts to reduce the growth rate.

The purpose of this study was to analyze the electron measurements of MMS in regions near the X-line of two magnetotail reconnection events to characterize the interactions leading to UH and both parallel and perpendicular beam-mode wave growth. It is found that crescent-shaped distributions with significant positive  $df/dv_{perp}$  produce UH wave growth and that multiple crescents, as reported for a reconnection event in the magnetotail by Torbert et al. (2018), produce UH waves with multiple growth rates that coexist with beam-mode waves at lower frequencies, leading to the broad frequency spectrum observed by MMS. Monidirectional parallel electron beams are shown to produce positive wave growth of beam-mode waves in the vicinity of a magnetotail X-line. The frequencies of these latter waves are downshifted from the plasma frequency ( $F_{pe}$ ) as expected for the relatively high ratio of beam density to background plasma density ( $\sim 0.25$ ; Cairns, 1989; Fuselier et al., 1985).

## 2. Data and Methods

An overview of the objectives and measurements of MMS is provided by Burch, Moore, et al. (2016). Phase 1 of MMS investigated reconnection along the dayside magnetopause and was followed by the investigation of tail reconnection in Phase 2. During Phase 2 the 28°-inclination elliptical orbit had apogee and perigee of 25  $R_E$  and 1.08  $R_E$ , respectively. During the time period of the study the four spacecraft were maintained in a tetrahedral configuration with average separations between 20 and 40 km throughout the “region of interest” defined as  $X_{gse} < -15 R_E$  within the magnetotail. The research reported here involves analysis of two tail reconnection events—one on 3 July 2017 near 05:26:50 UT and the other on 11 July 2017 near 22:34:02 UT (Torbert et al., 2018).

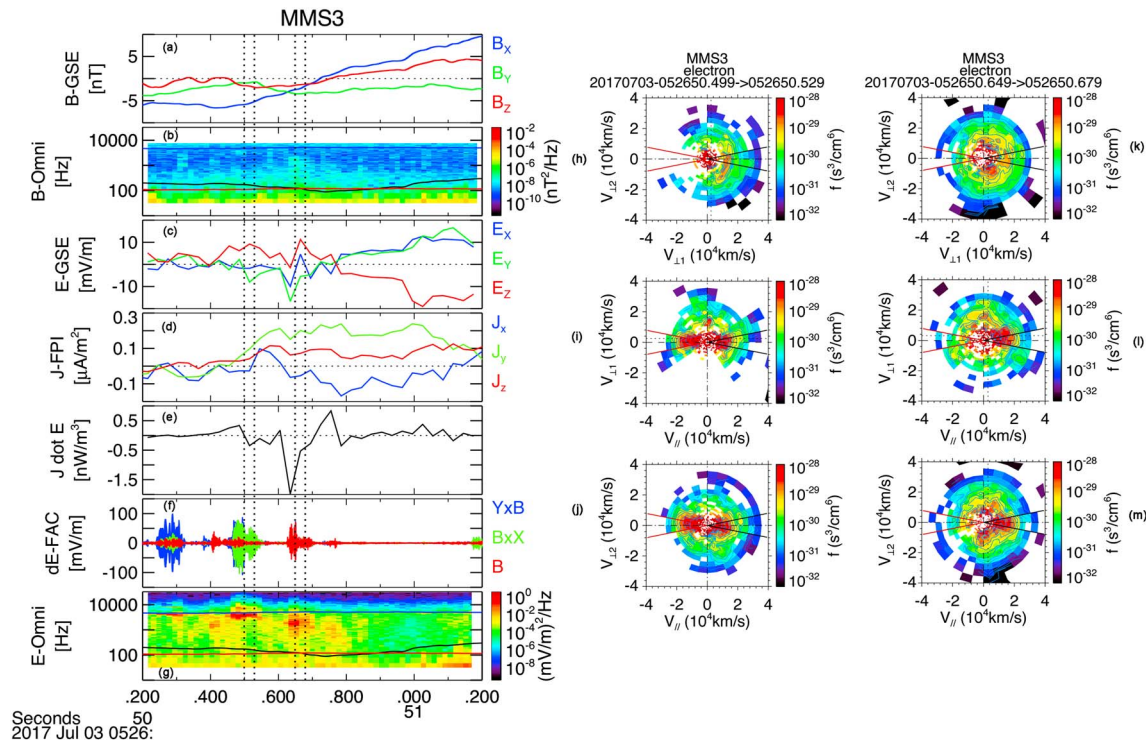
Data from only the MMS3 spacecraft were used in the analysis of both events because similar wave phenomena were observed by the other MMS spacecraft. The data sets included vector DC and AC electric and magnetic fields (Torbert et al., 2014) and 3-D plasma (Pollock et al., 2016). The electron measurements were modeled by multiple 3-D drifting bi-Maxwellian distributions, which were used in a linear dispersion analysis using the PDRK program (Xie & Yong, 2016).

## 3. Results

### 3.1. The 3 July 2017 Event

Figure 1 is a plot of plasma and field parameters from the MMS3 spacecraft for a 1-s period starting at 05:26:50.2 UT on 3 July 2017. The reconnection X-line is estimated to have been approached near 05:26:50.72 UT based on the reversals of  $B_x$  and  $B_z$  in panel (a). As is typical for magnetotail X-lines, which move rapidly tailward, the regions of Figure 1 to the left and right of the X-line are tailward and Earthward of the X-line, respectively. Panel (c) shows the GSE components of the DC electric field, while panel (d) shows the components of the current measured by the Fast Plasma Investigation. As shown in panel (e) the maximum positive energy conversion rate (measured by  $\mathbf{J} \cdot \mathbf{E}$ ) occurred toward the Earthward side of the X-line where wave activity was relatively weak, while the strongest wave emissions occurred toward its tailward side where  $\mathbf{J} \cdot \mathbf{E}$  was mostly negative. The bipolar signature of  $\mathbf{J} \cdot \mathbf{E}$  is commonly observed by MMS, particularly at the dayside magnetopause (Burch, Webster, et al., 2018; Swisdak et al., 2018). Panels (b) and (g) show the wave power spectral density for the AC magnetic and electric fields, respectively. Panel (f) shows AC electric field components in magnetic field-aligned coordinates.

In Figure 1 the two pairs of vertical dashed lines denote intervals containing (1) narrow-band waves near and above  $F_{pe}$  (and  $F_{uh}$ ) and (2) broadband waves peaked significantly below  $F_{pe}$ . Comparison of panels (b) and (g) shows that the waves at the first pair of vertical lines (location 1) were electrostatic while those at the second pair of vertical lines (location 2) had a small yet significant magnetic component. Panel (f) shows that the narrow-band waves at location 1 were strongest in the directions perpendicular to  $\mathbf{B}$ , indicating upper-hybrid waves, while at location 2 the oscillations were mainly parallel to  $\mathbf{B}$ . Also



**Figure 1.** Data from MMS3 on 3 July 2017. (a) Vector magnetic field components, (b) magnetic power spectral density, (c) DC electric field ( $\mathbf{E}$ ), (d) current from Fast Plasma Investigation, (e)  $\mathbf{J} \cdot \mathbf{E}$  from panels (c) and (d), (f) AC  $\mathbf{E}$  in magnetic field-aligned coordinates, (g) electric power spectral density, (h) electron distribution function at time noted by the first pair of vertical dashed lines in the left panel in plane normal to  $\mathbf{B}$  with  $V_{\text{perp}1} = (\mathbf{b} \times \mathbf{v}) \times \mathbf{b}$  direction (proxy for  $\mathbf{E} \times \mathbf{B}$ ), and  $V_{\text{perp}2} = -\mathbf{v} \times \mathbf{b}$ . (i) same as (h) except in plane containing  $\mathbf{B}$  with vertical axis along  $V_{\text{perp}1}$ . (j) same as (i) except for vertical axis along  $V_{\text{perp}2}$ . (k), (l), and (m) same as (h), (i), and (j) except for time noted by the second pair of vertical dashed lines in the left panel. The upper blue trace in the wave spectrograms is  $F_{\text{pe}}$  (essentially equal to  $F_{\text{uh}}$ ). The lower black trace is the electron cyclotron frequency. The red trace is ion plasma frequency. The position of MMS3 in Earth radii in GSE coordinates was:  $X = -17.5$ ,  $Y = 3.1$ ,  $Z = 2.1$ .

seen in panel (g) is the second harmonic, which appears just above  $F_{\text{pe}}/F_{\text{uh}}$  shortly before the time of location 1.

Electron DFs for the 30 ms time periods of locations 1 and 2 are shown in Figures 1h–1m. Each DF is a slice through the 3-D distribution averaged over  $\pm 20^\circ$  normal to the plane of the plot. The top plot is in the plane perpendicular to  $\mathbf{B}$ . The bottom two plots for each location are in the planes containing  $\mathbf{B}$  and  $V_{\text{perp}1}$  and  $\mathbf{B}$  and  $V_{\text{perp}2}$ , respectively. On each DF two sectors (black and red) are plotted along the central horizontal axis. In order to produce 1-D distributions (red line plots in Figure 2) the DF values are averaged over these sectors.

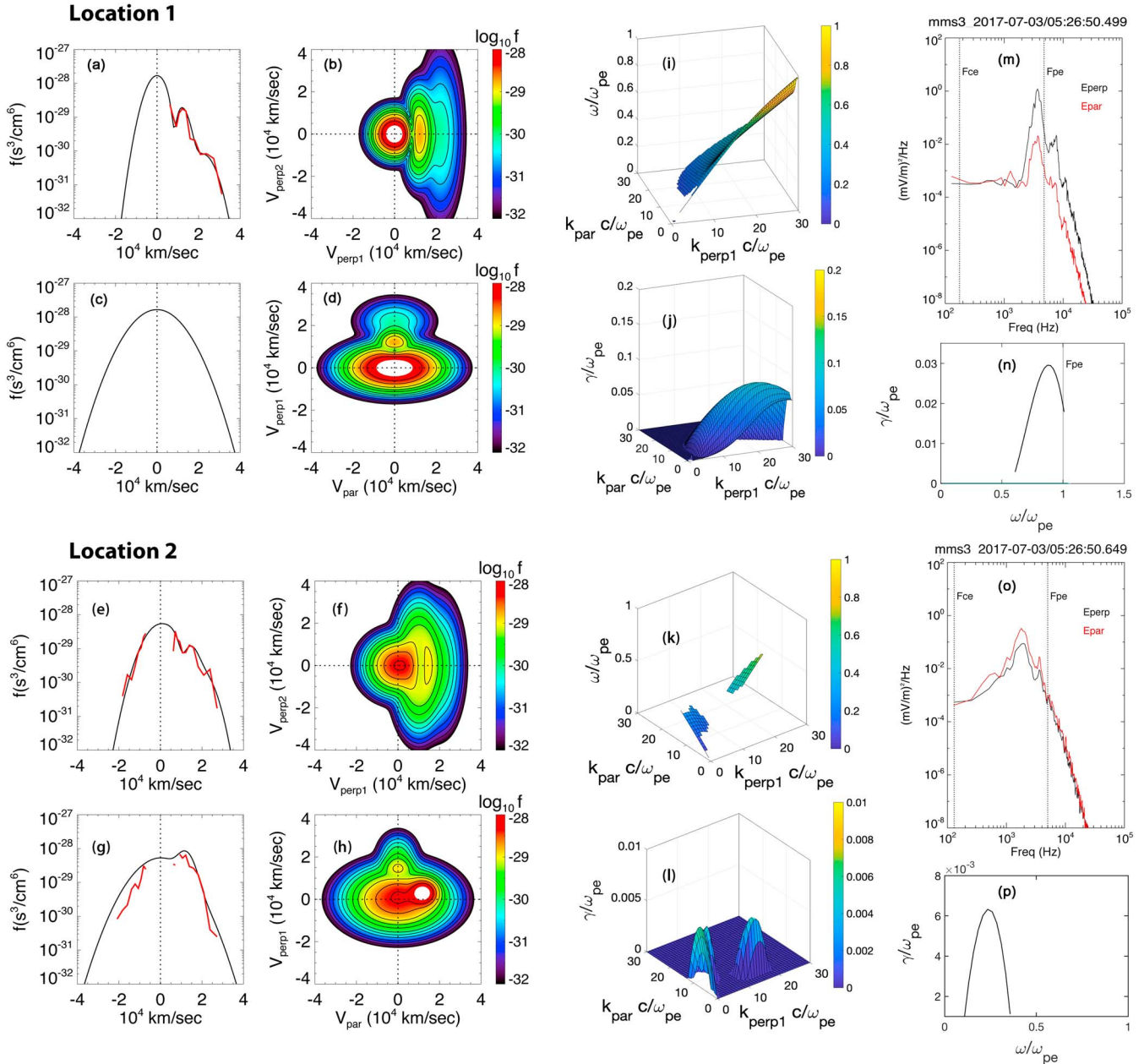
We note that the two top plots (DF perpendicular to  $\mathbf{B}$ ) show significant agyrotropy along  $+V_{\text{perp}1}$ , but the plot for location 1 contains a much more evident crescent-shaped distribution and a steep density gradient ( $df/dV_{\text{perp}1}$ ) at the inner edge of the crescent. The bottom two plots for location 1 (panels i and j) contain counterstreaming field-aligned electrons while the two plots for location 2 (panels l and m) contain a monodirectional beam along  $+\mathbf{B}$ . As will be shown in the forthcoming analysis, significant wave growth is associated with the perpendicular crescent at (1) and both the perpendicular agyrotropy and monodirectional parallel beam at (2).

The complete set of magnetic field, wave, and electron DF data for this time interval is shown in movie format in the supporting information (SI, Movie S1). Also shown in the SI is a polarization analysis for the 3 July 2017 event, which supports the conclusion that UH waves occurred at location 1 while beam-mode waves occurred at location 2.

### 3.1.1. Wave Analysis

In order to evaluate the measured electron DFs as possible sources of the observed waves we performed linear dispersion analyses using the PDRK kinetic dispersion relation solver (Xie & Yong, 2016). Our inputs to

Event 1 3 July 2017



**Figure 2.** Dispersion analysis for the two wave locations on 3 July 2017. (a–d) Model distribution for location 1 (Table 1) with 1-D distribution function slice and 2-D contour plot in planes normal and parallel to **B**. Red trace in panel (a) is from distribution function averaged within the angular sectors shown in Figure 1h. (e–h) same as panel (a)–(d) except for second wave location in Figure 1(k–m). (i–l) Dispersion analyses for locations 1 and 2 with dispersion relations shown in panels (i) and (k) and growth rate versus wave number shown in panels (j) and (l). (m) Parallel and perpendicular components of observed wave spectrum for location 1. (n) Wave growth versus freq. for location 1 (linear scale). (o) Same as panel (m) but for location 2. (p) Same as panel (n) but for location 2.

PDRK consisted of multiple bi-Maxwellian populations with flows along and normal to **B**. Following the approach of Sundkvist et al. (2005) we utilized negative densities to produce shell or crescent-type distributions.

Table 1 shows the parameters used to fit the various DFs used in this study. The first two sets of parameters are for locations 1 and 2, shown in Figure 1. For both locations multiple drifting bi-Maxwellian distributions were needed to model the 3-D observations. Note that for location 1 the modeled distribution includes a bullet-shaped core distribution, an inner crescent that includes both a positive and a negative density

**Table 1**  
*Parameters of Maxwellian Distribution Fits to Electron Distribution Functions*

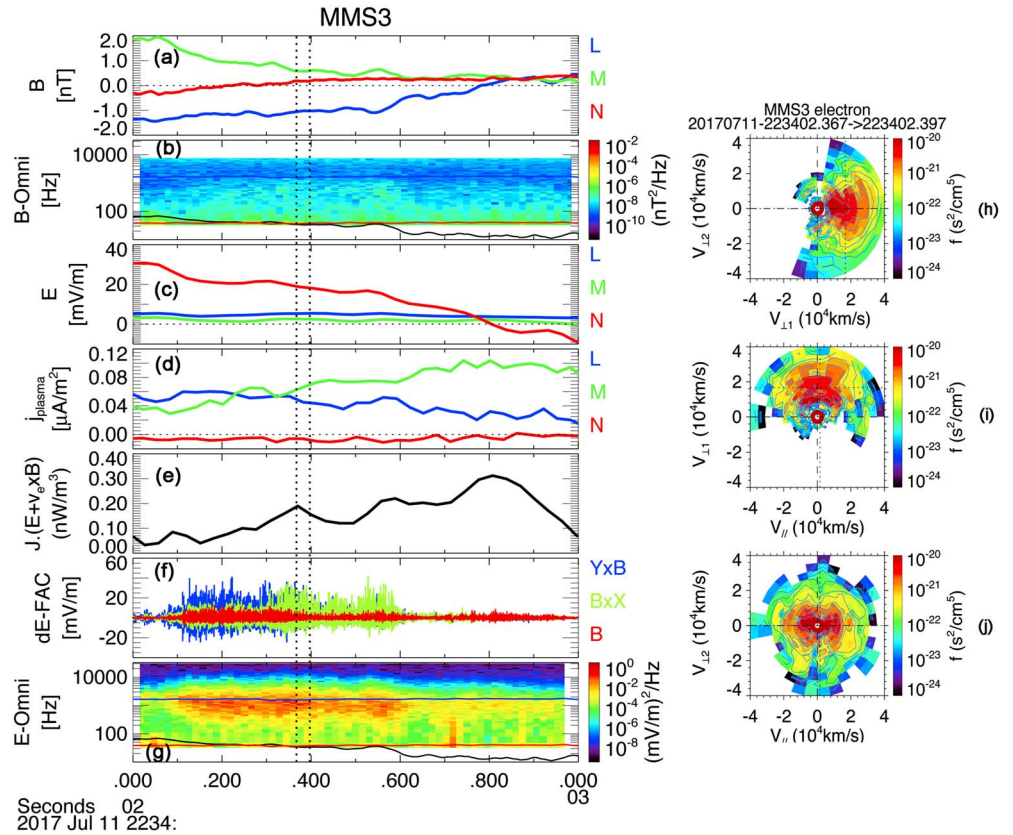
Drifting Maxwellian components	Density ( $\text{cm}^{-3}$ )	Drift velocity ( $10^4$ km/s)			Thermal velocity ( $10^4$ km/s)		
		$V_{\text{Par}}$	$V_{\text{Perp1}}$	$V_{\text{Perp2}}$	$V_{\text{Par}}$	$V_{\text{Perp1}}$	$V_{\text{Perp2}}$
3 July 2017 location 1							
Core	0.35	0.0	0.0	0.0	1.20	0.55	0.55
Inner crescent	0.026	0.0	1.15	0.0	0.50	0.40	1.10
Inner crescent (negative density)	-0.018	0.0	0.73	0.0	0.55	0.31	0.70
Outer crescent	0.006	0.0	2.20	0.0	1.0	0.60	2.20
3 July 2017 location 2							
Core	0.2016	0.0	0.0	0.0	1.25	0.78	0.70
Parallel beam	0.0512	1.20	0.30	0.0	0.45	0.40	0.30
Crescent	0.1100	0.0	1.00	0.0	0.50	0.57	1.40
Crescent (negative density)	-0.068	0.0	0.99	0.0	0.50	0.435	1.10
High-energy component	0.005	0.0	2.0	0.0	0.50	0.60	1.60
11 July 2017							
Core (parallel beam)	0.0068	1.24	0.90	0.0	0.40	0.40	0.40
Core (antiparallel beam)	0.0122	-0.70	0.90	0.0	0.90	0.30	0.40
Inner crescent	0.0207	0.0	1.70	0.0	0.80	0.60	0.80
Inner crescent (negative density)	-0.0099	0.0	1.40	0.0	0.90	0.90	0.60
Outer crescent	0.0203	0.0	2.50	0.0	1.40	1.00	1.50
Outer crescent (negative density)	-0.0142	0.0	2.20	0.0	1.20	0.70	1.30

component, and an outer crescent. Location 2 contains a core distribution, the monodirectional field-aligned (parallel) beam and the crescent that was observed in the plane perpendicular to  $\mathbf{B}$ , and a higher-energy component.

Table 1 shows the parameters for bi-Maxwellian inputs to linear dispersion analysis of the three wave events analyzed in this study. Thermal velocities and beam velocities are shown for three directions:  $V_{\text{par}}$  = parallel to  $\mathbf{B}$ ,  $V_{\text{perp1}} = (\mathbf{b} \times \mathbf{v}) \times \mathbf{b}$  (proxy for  $\mathbf{E} \times \mathbf{B}$ ), and  $V_{\text{perp2}} = -\mathbf{v} \times \mathbf{b}$ , where  $\mathbf{b}$  and  $\mathbf{v}$  are unit vectors of the magnetic field and the electron velocity moment, respectively.

Figure 2 shows the modeled electron DFs (a–h), the result of the linear dispersion analysis (i–l), and the observed and predicted frequency spectra for locations 1 and 2 (m–p). Shown in panels (a), (e), and (g) in red are observed 1-D DF traces averaged over the black and red sectors plotted in the DFs in Figures 1h, 1k, and 1l. For location 1 the dispersion relation shown in panel (j) has the typical shape of an electrostatic beam-mode instability (Dum, 1989), and the resulting growth rate versus wave number relation shows positive wave growth at large  $k_{\text{perp}}$  and small  $k_{\text{par}}$ . The predicted growth rate versus frequency relation in Figure 2n shows a peak near  $0.8 \omega_{\text{pe}}$ , which agrees with the observed fundamental peak in Figure 2m. The harmonics that appear in panel (m) are not reproduced by the linear analysis of PDRK because they result from nonlinear effects (e.g., Klimas, 1983; Yoon et al., 2003).

The results of the dispersion analysis for location 2 are shown in the bottom half of Figure 2. The measured 1-D DFs averaged over the black and red sectors in Figures 1k and 1m are plotted by the red traces in Figures 2e and 2g. For this location there is a positive  $df/dv$  both parallel and perpendicular to  $\mathbf{B}$ . As is the case for WHAMP (Rönmark, 1983) and other linear dispersion solvers, the PDRK code only handles parallel (to  $\mathbf{B}$ ) beams or unmagnetized plasmas. Thus, we ran a separate analysis for the perpendicular (to  $\mathbf{B}$ ) beam (assuming a parallel (to  $\mathbf{B}$ ) beam) and plot the parallel and perpendicular beam results together in Figures 2k and 2l. As shown in Figure 2k, both solutions showed typical beam-mode dispersion relations. The growth-rate surfaces in Figure 2l show that while both beams resulted in wave growth, the parallel beam growth rate was somewhat larger. This difference is confirmed by the measured wave spectrum in Figure 2o with the parallel component being stronger for both the fundamental and second harmonic. The derived frequency spectrum in Figure 2p shows a peak at slightly lower frequency than observed ( $\sim 0.25 F_{\text{pe}}$  vs  $\sim 0.35 F_{\text{pe}}$ ). The position of the frequency peaks significantly below  $F_{\text{pe}}$  results from the relatively high value of the beam density relative to the background plasma density, which was  $\sim 0.25$  for the parallel beam (Table 1). This type of downshift was reported for foreshock electron oscillations by Fuselier et al. (1985) and is in approximate agreement with the theoretical predictions of Cairns (1989).



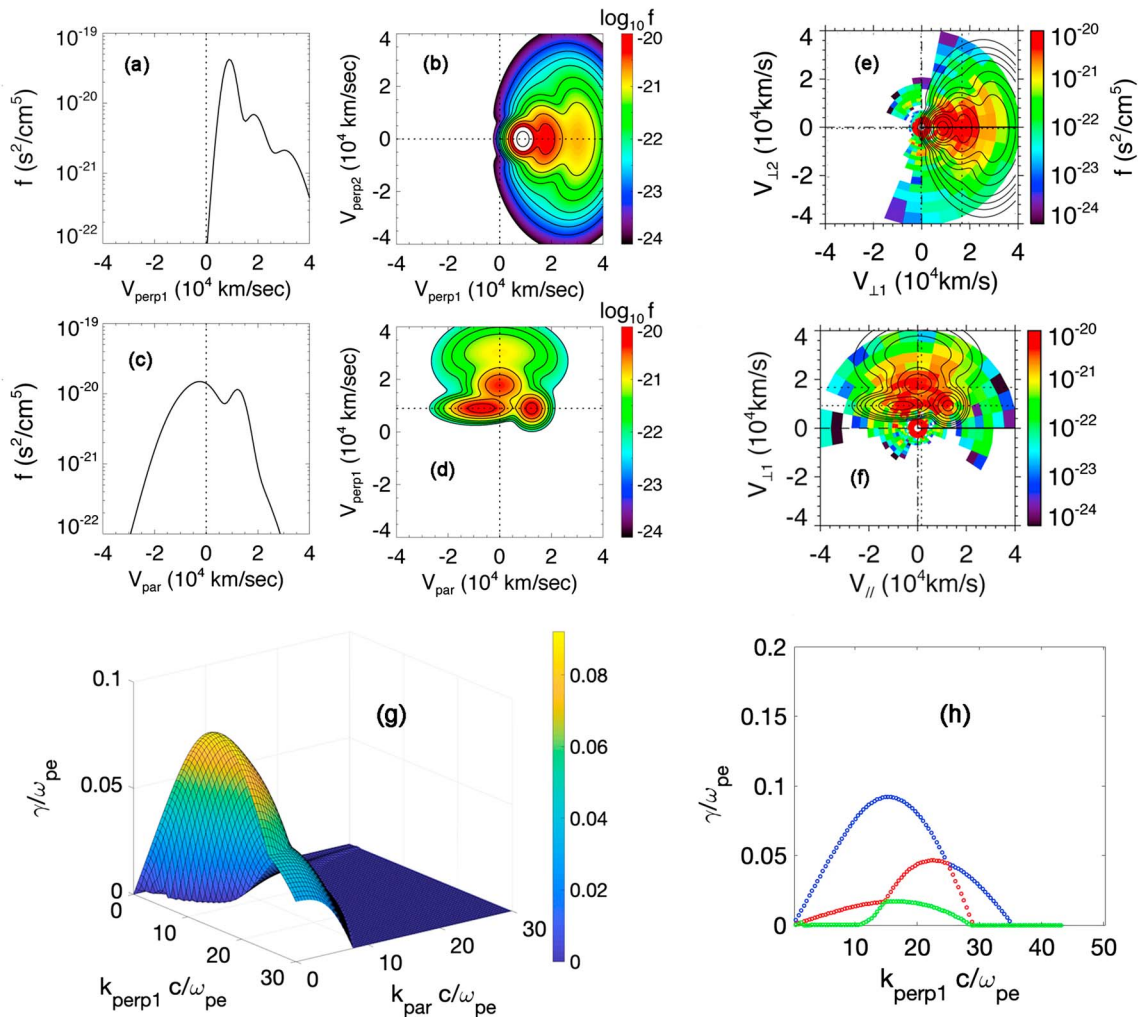
**Figure 3.** Same as Figure 1 except for event on 11 July 2017 when the position of MMS3 in  $R_E$  in GSE coordinates was:  $X = -21.5$ ,  $Y = 4.2$ ,  $Z = 3.6$ . For this event the plots in panels (h)–(j) are reduced distribution functions, which are summed over the axis normal to the plane of each plot. Boundary-normal coordinates are used where [L, M, N] in GSE coordinates are: [0.971, 0.216,  $-0.106$ ;  $-0.234$ , 0.948,  $-0.215$ ; 0.054, 0.233, 0.971] as derived by Torbert et al. (2018).

As an additional check, the DF centered at 05:26:51.024 UT was modeled and analyzed using PDRK with no wave growth produced. This negative result is in agreement with the wave spectrogram shown in Figure 1f.

### 3.2. The 11 July 2017 Event

Another tail reconnection event on 11 July 2017 has been reported by Torbert et al. (2018), who noted the occurrence of UH waves in the presence of multiple electron crescent distributions. Figure 3 shows a subset of the data for a 1-s interval during that event. The data format is the same as for Figure 1 with a reconnection X-line identified from the reversal of  $B_N$  in panel (a), near 22:34:02.85 UT. As shown in Figure 3e,  $\mathbf{J} \cdot (\mathbf{E} + \mathbf{v}_e \times \mathbf{B})$  or  $\mathbf{J} \cdot \mathbf{E}'$  was mostly positive during the event with a peak in the region of enhanced waves at  $\sim F_{pe}$ , shown by the electric field component in panel (g). Comparison to the magnetic field spectrogram in panel (b) shows the enhanced waves to be quasi-electrostatic. Panel (f) plots the AC electric field in field-aligned coordinates, which shows the wave oscillations to be mainly directed perpendicular to  $\mathbf{B}$ . The pair of dashed vertical lines in Figure 1 show the time period for the DFs plotted in panels (h)–(j). In this case, because of the much lower count rates compared to the 3 July events reduced DFs are used with the data summed over the axis normal to plane of the plot. As noted by Torbert et al. (2018), the DF in Figure 3h shows three structures (a drifting core and two crescents). We calculated  $\mathbf{J} \cdot \mathbf{E}'$  separately for three energy ranges covering these three structures: electron bins 9–17 (73.6–634.5 eV), bins 17–21 (634.5–1863.16 eV), and bins 21–24 (1863.16–4179.2 eV). For calculation of currents, ion bins 10–17 (77.98–556.22 eV), bins 17–21 (556.22–1709.37 eV), and bins 21–24 (1709.37–3967.62 eV) were also needed. Fractional contributions to  $\mathbf{J} \cdot \mathbf{E}'$  were found to be 0.0942 for the core, 0.532 for the inner crescent, and 0.374 for the outer crescent.

Event 2 11 July 2017



**Figure 4.** (a–d) as in Figure 2 except for reduced DFs, 1-D line plots and 2-D contour plots of a six bi-Maxwellian model for 11 July 2017 in Table 1. (e–f) Model contours overlaid on reduced DF plots from Figures 3h–3i. (g) Growth rate versus wave numbers. (h) Growth rate versus frequency for three DF components: At  $k_{\text{perp1}} = 0$  bullet-shaped core (green), inner crescent (red), and outer crescent (blue). At  $k_{\text{perp1}} > 0$  highest growth rate (blue), medium (red), lowest (green). DF = distribution function.

The complete set of magnetic field, plasma, and wave data for this time interval is shown in movie format in the SI (Movie S2). Also shown in the SI is a polarization analysis for the 11 July 2017 event, which supports the conclusion that UH waves occurred at the time of the multiple crescent distribution shown in Figure 3.

**3.2.1. Wave Analysis**

Figure 4 shows the results of the PDRK dispersion analysis for the 11 July 2017 event, which was modeled by six drifting bi-Maxwellian distributions as listed in Table 1. Figures 4a–4d plot 1-D reduced DFs averaged over the same angular sectors shown in Figure 1 along with contour plots of reduced DFs taken from the third model listed in Table 1. Figures 4e and 4f plot the model contours from panel (b) overlaid on the reduced DFs from Figures 3h and 3i after first removing the data contours. Figure 4g is a surface plot of growth rate versus wave number showing significant wave growth in the perpendicular direction. Figure 4h shows three distinct traces of wave growth rate versus frequency, which are associated with the core distribution (medium growth rate), the inner crescent (lowest growth rate), and the outer crescent (highest growth rate). The color codes in panel (h) indicate these three levels at each  $k_{\text{perp1}}$  value in green, red, and blue, respectively. The predicted frequency spectrum is therefore fairly broad as observed in

Figure 3g. The dispersion relation for this event, although not shown here, has the characteristic beam-mode shape as found for events 1 and 2 in Figure 2.

#### 4. Conclusions

Waves near the electron plasma frequency are reported for two magnetotail neutral-sheet crossings, both of which had signatures of reconnection including magnetic field reversals, electron crescent distributions, monodirectional electron beams, and positive  $\mathbf{J} \cdot \mathbf{E}$  or  $\mathbf{J} \cdot \mathbf{E}'$ . MMS observed high-frequency wave emissions with characteristics of UH waves (wave oscillations near  $90^\circ$ ) and beam-mode waves (wave oscillations near  $0^\circ$ ) slightly displaced toward the tailward exhaust of each event. The parallel beam-mode wave frequencies were downshifted from  $F_{pe}$  because of the high ratio between beam density and background plasma density as reported by Fuselier et al. (1985) and Cairns (1989). Linear dispersion analysis shows that both types of waves are generated by beam-plasma interactions with the UH waves resulting from crescent distributions, as observed previously in dayside magnetopause reconnection events by Graham et al. (2017). The parallel waves are shown to be caused by monodirectional beams.

In the event on 11 July 2017, the dispersion analysis found separate solutions for the drifting core distribution, an inner crescent, and an outer crescent distribution resulting in a significant frequency spread as was observed by MMS. Significant power existed at harmonics of the fundamental frequency for both the UH and parallel beam-mode waves, but the harmonics are not predicted by linear analysis because they result from nonlinear effects.

#### Acknowledgments

This work was supported by NASA contract NNG04EB99C at SwRI. K. J. H. and K. D. were supported in part by NSF AGS-1602510, NASA grants 80NSSC18K1337, 80NSSC18K1534, 80NSSC18K0570, 80NSSC18K0693, and the ISSI program: MMS and Cluster observations of magnetic reconnection. O. L. C. was supported by CNES and CNRS. The entire MMS data set is available online (at <https://lasp.colorado.edu/mms/sdc/public/links/>). Fully calibrated data are placed online at this site within 30 days of their transmission to the MMS Science Operations Center. The data are archived in the NASA Common Data Format (CDF) and so can be plotted using a number of different data display software packages that can use CDF files. A very comprehensive system called the Space Physics Environment Data Analysis System (SPEDAS) is available by downloading [http://themis.ssl.berkeley.edu/socware/bleeding\\_edge/](http://themis.ssl.berkeley.edu/socware/bleeding_edge/) and selecting `spds_w_latest.zip`. Training sessions on the use of SPEDAS are held on a regular basis at space physics related scientific meetings. All of the data plots in this paper were generated with SPEDAS software applied to the publicly available MMS data base, so they can readily be duplicated. It is a pleasure to thank Hua-sheng Xie for providing his PDRK code and for very helpful suggestions on using it. The PDRK code, along with extensive documentation is found online (at <https://github.com/hsxie/pdrk>). Many thanks are also due to Stephen Kreisler of GSFC who computed the partial electron and ion moments.

#### References

- Burch, J. L., Ergun, R. E., Cassak, P. A., Webster, J. M., Torbert, R. B., Giles, B. L., et al. (2018). Localized oscillatory energy conversion in magnetopause reconnection. *Geophysical Research Letters*, *45*(3), 1237–1245. <https://doi.org/10.1002/2017GL076809>
- Burch, J. L., Moore, T. E., Torbert, R. B., & Giles, B. L. (2016). Magnetospheric multiscale overview and science objectives. *Space Science Reviews*, *199*(1-4), 5–21. <https://doi.org/10.1007/s11214-015-0164-9>
- Burch, J. L., & Phan, T. D. (2016). Magnetic reconnection at the dayside magnetopause: Advances with MMS. *Geophysical Research Letters*, *43*, 8327–8338. <https://doi.org/10.1002/2016GL069787>
- Burch, J. L., Torbert, R. B., Phan, T. D., Chen, L.-J., Moore, T. E., Ergun, R. E., et al. (2016). Electron-scale measurements of magnetic reconnection in space. *Science*, *352*(6290), aaf2939. <https://doi.org/10.1126/science.aaf2939>
- Burch, J. L., Webster, J. M., Genestreti, K. J., Torbert, R. B., Giles, B. L., Fuselier, S. A., et al. (2018). Wave phenomena and beam-plasma interactions at the magnetopause reconnection region. *Journal of Geophysical Research: Space Physics*, *123*, 1118–1133. <https://doi.org/10.1002/2017JA024789>
- Cairns, I. H. (1989). Electrostatic wave generation above and below the plasma frequency by electron beams. *Physics of Fluids B: Plasma Physics*, *1*(1), 204–213. <https://doi.org/10.1063/1.859088>
- Dum, C. T. (1989). Transition in the dispersive properties of beam-plasma and two-stream instabilities. *Journal of Geophysical Research*, *94*(A3), 2429–2442. <https://doi.org/10.1029/JA094iA03p02429>
- Farrell, W. M., Desch, M. D., Kaiser, M. L., & Goetz, K. (2002). The dominance of electron plasma waves near a reconnection X-line region. *Geophysical Research Letters*, *29*(19), 1902. <https://doi.org/10.1029/2002GL014662>
- Farrell, W. M., Desch, M. D., Ogilvie, K. W., Kaiser, M. L., & Goetz, K. (2003). The role of upper hybrid waves in magnetic reconnection. *Geophysical Research Letters*, *30*(24), 2259. <https://doi.org/10.1029/2003GL017549>
- Fuselier, S. A., Gurnett, D. A., & Fitzenteiter, R. J. (1985). The downshift of electron plasma oscillations in the electron foreshock region. *Journal of Geophysical Research*, *90*(A5), 3935–3946. <https://doi.org/10.1029/JA090iA05p03935>
- Graham, D. B., Khotyaintsev, Y. V., Vaivads, A., Norgren, C., André, M., Webster, J. M., et al. (2017). Instability of agyrotropic electron beams near the electron diffusion region. *Physical Review Letters*, *119*(2). <https://doi.org/10.1103/PhysRevLett.119.025101>
- Graham, D. B., Vaivads, A., Khotyaintsev, Y. V., André, M., le Contel, O., Malaspina, D. M., et al. (2018). Large-amplitude high-frequency waves at Earth's magnetopause. *Journal of Geophysical Research: Space Physics*, *123*, 2630–2657. <https://doi.org/10.1002/2017JA025034>
- Hoshino, M., Hiraide, K., & Mukai, T. (2001). Strong electron heating and non-Maxwellian behavior in magnetic reconnection. *Earth, Planets and Space*, *53*(6), 627–634. <https://doi.org/10.1186/BF03353282>
- Klimas, A. J. (1983). A mechanism for plasma waves at the harmonics of the plasma frequency in the electron foreshock boundary. *Journal of Geophysical Research*, *88*(A11), 9081–9091. <https://doi.org/10.1029/JA088iA11p09081>
- Oieroset, M., Phan, T. D., Fijimoto, M., Lin, R. P., & Lepping, R. P. (2001). In-situ detection of collisionless reconnection in the Earth's magnetotail. *Nature*, *412*(6845), 414–417. <https://doi.org/10.1038/35086520>
- Pollock, C. J., Moore, T., Jacques, A., Burch, J., Gliese, U., Saito, Y., et al. (2016). Fast plasma investigation for magnetospheric multiscale. *Space Science Reviews*, *199*(1-4), 331–406. <https://doi.org/10.1007/s11214-016-0245-4>
- Rönmark, K. (1983). Computation of the dielectric tensor of a Maxwellian plasma. *Plasma Physics*, *25*(6), 699–701. <https://doi.org/10.1088/0032-1028/25/6/007>
- Sundkvist, D., Vaivads, A., André, M., Wahlund, J. E., Hobar, Y., Joko, S., et al. (2005). Multi-spacecraft determination of wave characteristics near the proton gyrofrequency in high-altitude cusp. *Annales Geophysicae*, *23*(3), 983–995. <https://doi.org/10.5194/angeo-23-983-2005>
- Swisdak, M., Drake, J. F., Price, L., Burch, J. L., Cassak, P. A., & Phan, T.-D. (2018). Localized and intense energy conversion in the diffusion region of asymmetric magnetic reconnection. *Geophysical Research Letters*, *45*, 5260–5267. <https://doi.org/10.1029/2017GL076862>



- Torbert, R. B., Burch, J. L., Phan, T. D., Hesse, M., Argall, M. R., Shuster, J., et al. (2018). Electron-scale dynamics of the diffusion region during symmetric magnetic reconnection in space. *Science*, *362*(6421), 1391–1395. <https://doi.org/10.1126/science.aat2998>
- Torbert, R. B., Russell, C. T., Magnes, W., Ergun, R. E., Lindqvist, P.-A., LeContel, O., et al. (2014). The FIELDS instrument suite on MMS: Scientific objectives, measurements, and data products. *Space Science Reviews*, *199*(1-4), 105–135. <https://doi.org/10.1007/s11214-014-0109-8>
- Xie, H., & Yong, X. (2016). PDRK: A general kinetic dispersion relation solver for magnetized plasma. *Plasma Science and Technology*, *18*(2), 97–107. <https://doi.org/10.1088/1009-0630/18/2/01>
- Yoon, P. H., Gaelzer, R., Umeda, T., Omura, Y., & Matsumoto, H. (2003). Harmonic Langmuir waves. I. Nonlinear dispersion relation. *Physics of Plasmas*, *10*(2), 364–372. <https://doi.org/10.1063/1.1537238>